

Gain compression in Josephson Traveling-Wave Parametric Amplifiers

Gwenael Le Gal,¹ Guilliam Butseraen,^{1,*} Arpit Ranadive,^{1,†} Giulio Cappelli,¹ Bekim Fazlili,^{1,2} Edgar Bonet,¹ Eric Eyraud,¹ Luca Planat,² and Nicolas Roch^{1,2,‡}

¹ Univ. Grenoble Alpes, CNRS, Grenoble INP, Institut Néel, 38000 Grenoble, France

² Silent Waves, 38000 Grenoble, France

Superconducting traveling-wave parametric amplifiers (TWPAs) are increasingly used in various applications, including quantum computing, quantum sensing, and dark matter detection. However, one important characteristic of these amplifiers, gain compression, has not received much attention. As a result, there is a lack of comprehensive experimental exploration of this phenomenon in the existing literature. In this study, we present an experimental investigation of gain compression in a Josephson traveling-wave parametric amplifier based on a four-wave mixing process. We have implemented a novel setup to monitor the complex transmission of both the pump and signal tones, which allows us to simultaneously track pump depletion and signal amplification as functions of signal power and frequency across the entire bandwidth of the device. Our findings indicate that, while pump depletion occurs during gain compression, it is not the only mechanism involved in the saturation of a TWPA. Power-induced phase-matching processes also take place within the device. This study provides valuable insights for optimizing TWPAs for applications that require high total input power, such as multiplexed qubit readout or broadband photon emission.

I. INTRODUCTION

Superconducting traveling-wave parametric amplifiers can be constructed using high-kinetic inductance materials (K-TWPA) [1] or Josephson junction arrays (J-TWPA) [2]. These amplifiers provide bandwidths extending to several GHz, achieve gains of ~ 20 dB, and exhibit noise characteristics approaching the quantum limit. Additionally, TWPAs can be located directly at the coldest stage of dilution refrigerators because of their limited power dissipation. This placement minimizes the losses between the device under test and the TWPA, thus improving the signal-to-noise ratio (SNR) of the detection [3]. Collectively, these benefits have established TWPAs as essential amplifiers in circuit quantum electrodynamics (cQED) experiments, facilitating high-fidelity readout of superconducting [4–10] and semiconducting qubits [11, 12], and significantly increasing the SNR in quantum optics experiments [13, 14].

A fundamental attribute of any amplifier is its saturation power, defined as the input signal power at which a deviation from linear gain emerges. The 1-dB compression point $P_{1\text{dB}}$ serves as a prevalent metric to assess the saturation of the amplifier. This point is the input signal power at which the amplifier's gain experiences a 1-dB reduction. A high $P_{1\text{dB}}$ is particularly advantageous for applications that require substantial total input power, such as in the multiplexed readout of superconducting qubits [5, 15] or spin qubits [12]. Resonant Josephson parametric amplifiers (JPAs) [16], representing another class of near-quantum-limited amplifiers, generally exhibit 1-dB compression points below -120 dBm [17, 18]. However,

enhanced JPA designs can achieve saturation powers that reach -90 dBm [19–21]. This advancement is attributed to the diluted non-linearity provided by arrays of Josephson junctions, or composite elements [18, 20–24], as well as the attenuation of higher-order nonlinear effects of the Josephson potential [25–27].

The 1-dB compression point $P_{1\text{dB}}$ ranges from -110 to -95 dBm for J-TWPA [2, 4, 28, 29], while K-TWPA can reach -50 dBm [30]. The difference between JPAs and TWPAs can be understood by examining the ratio of non-linearity K to bandwidth κ [18, 22]. Most JPAs typically consist of around one hundred nonlinear elements, whereas TWPAs are usually made up of thousands of such components—Josephson junctions in the case of J-TWPA and squares for K-TWPA. This design effectively distributes the non-linearity across all the elements, thereby reducing the value of K . Additionally, TWPAs offer a larger bandwidth compared to JPAs. Consequently, the ratio K/κ is more favorable for TWPAs when it comes to maximizing $P_{1\text{dB}}$. Despite the first demonstrations of TWPAs occurring over a decade ago [1, 4], a comprehensive experimental exploration of their saturation remains absent, to the best of our knowledge. Theoretical analyses have been focusing solely on the effect of pump depletion—a notable reduction in the pump tone's amplitude as energy is transferred to the signal and idler modes, to study saturation in TWPAs [31–33]. Another potential constraint on TWPA power handling is cross-phase modulation prompted by high-power signals. Analogous to observations in JPA, where a strong signal can cause deviation from optimal biasing conditions, a strong signal might impair the essential phase-matching of a TWPA. Further propagative effects have to be considered as well. The final potentially detrimental effect is the generation of spurious tones by the device, including harmonics [34], sidebands, or intermodulation products [15, 35]. Recent research on the generation of intermodulation products in a J-TWPA [15] has demonstrated

* Now at Silent Waves.

† Now at Google.

‡ Corresponding author: nicolas.roch@neel.cnrs.fr

that these unwanted tones can be harmful to multiplexed qubit readout and that their generation is intrinsically connected to the saturation properties of the amplifier, similar to what is observed in non-superconducting voltage amplifiers [35].

In this article, we conduct a comprehensive experimental study on gain compression in a J-TWPA. Although the 1-dB compression point of TWPA is usually measured and discussed at peculiar frequencies in the amplification band [2], we systematically measure the 1-dB compression point ($P_{1\text{dB}}$) throughout the amplifier bandwidth, anticipating significant variations due to frequency-dependent gain, which may also be affected by device imperfections and the microwave environment [36]. A novel measurement approach is introduced, which uses two vector network analyzers (VNA) to simultaneously measure the complex transmission of pump and signal tones. The article is structured as follows. Section II briefly explains the operating principle of the device under study, a TWPA constructed with Superconducting Nonlinear Asymmetric Inductive Elements (SNAIL) operating in the reversed-Kerr regime [29], along with the experimental setup. Section III discusses the theoretical framework used to model the data using the well-known coupled-mode equations [29, 31, 32, 37], comparing the results for the gain and pump transmission profiles. Section IV delves deeper into 1-dB gain compression and its correlation with pump depletion, but also other effects such as power-induced phase-mismatch. Lastly, in Section V, the broader implications of the results are discussed, along with strategies to address the current low-saturation power limitations of Josephson TWPA.

II. TRAVELING-WAVE PARAMETRIC AMPLIFICATION AND DESCRIPTION OF THE EXPERIMENT

This study examines the saturation characteristics of a J-TWPA operating within the four-wave mixing (4WM) regime. In this context, effective amplification is contingent on two conditions: energy conservation $2\omega_p = \omega_s + \omega_i$ and momentum conservation $2\tilde{k}_p = \tilde{k}_s + \tilde{k}_i$ among the pump p , signal s , and idler i tones. Here, \tilde{k}_j denotes a general wave vector that is frequency and power dependent. Whereas the rule of energy conservation is inherently satisfied, satisfying the second condition presents greater difficulty due to the inherent curvature of the dispersion relation in a Josephson Junction (JJ) array and the self- and cross-Kerr effects (or equivalently, the self- and cross-phase modulations), which results in power-dependent vectors \tilde{k} . It is critical to emphasize that momentum conservation can significantly influence the amplification characteristics of a TWPA, resulting in gain variations ranging from 10 dB to 20 dB between a device lacking momentum matching considerations and one that is meticulously engineered for such purposes, despite the nonlinear properties being identical [28, 37].

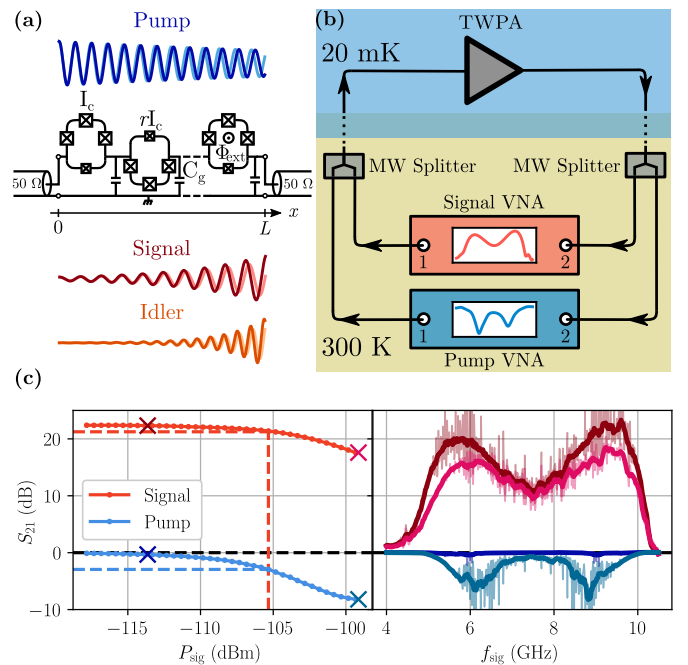


Figure 1. **1-dB compression in a TWPA.** (a) The device consists in a chain of SNAIL forming a $50\ \Omega$ matched non-linear transmission line. The device is flux biased at $\Phi_{\text{ext}} = \Phi_0/2$. A strong pump tone (blue) at frequency ω_p provides the energy to amplify the signal tone (red) at frequency ω_s and generate an idler tone (orange) at frequency $\omega_i = 2\omega_p - \omega_s$. The tones can experience a phase shift as they propagate due to self and cross-phase modulation effects (highlighted by the light-color waves), in addition to being amplified or attenuated. The amplitudes of all these effects are exaggerated for illustrative purposes. (b) Simplified schematic of the room temperature experimental setup. The microwave source usually used to generate the pump tone is replaced by a second VNA ('pump VNA'). (c) Examples of experimental curves obtained from the experimental setup shown in (b). Signal gain and pump transmission (red and blue, respectively) as a function of the input signal power P_{sig} (left panel) for $f_{\text{sig}} = 6\ \text{GHz}$ and $f_{\text{pump}} = 7.5\ \text{GHz}$, and versus signal frequency (right panel). The pump power is approximately $-78.4\ \text{dBm}$. The vertical dashed line shows $P_{1\text{dB}}$, and the blue horizontal dashed line highlights pump attenuation at $P_{\text{sig}} = P_{1\text{dB}}$. The dark colors correspond to $P_{\text{sig}} = -113.6\ \text{dBm}$, and the brighter colors to $P_{\text{sig}} = -99.3\ \text{dBm}$ (see corresponding colored crosses in the left panel). The light shades show the raw acquired data while the thicker plain lines show the smoothed transmission profiles.

The device under study here, whose schematic is shown in Fig. 1, is a SNAIL-based TWPA [38], operated in the 'reversed-Kerr' regime with an external DC flux bias $\Phi_{\text{ext}} = \Phi_0/2$ [29]. Momentum matching is obtained by reversing the sign of Kerr non-linearity, such that the power-induced modification of the \tilde{k} vectors compensates for the natural mismatch between the zero-power or linear k vectors.

As schematically depicted in Fig. 1(a), energy is drawn

from the pump to amplify the signal and generate the idler tone. The different waves also inherit a phase shift due to self- and cross-phase modulation effects as their amplitudes vary while they propagate and interact. In this picture, these phenomena can limit the achievable gain of the device for two reasons. First, as the amplitudes of the signal and idler waves increase, some pump power is irreversibly converted to ω_s and ω_i and less energy is available for amplification, until the gain saturates before the waves exit the TWPA (this effect is known as *pump depletion*). Second, as the wave amplitudes vary, momentum mismatch, or phase-mismatch, due to Kerr effects can increase, and the gain can also saturate inside the device because of decreasing interaction efficiency. This effect can be triggered by pump depletion.

In practice, it has already been shown that as long as the input signal power is small with respect to the pump one, such effects are negligible and optimal performance of the TWPA is achieved [29, 31, 32, 37]. However, when the input signal power is increased, the amplified signal tone inside the device can become a significant fraction of the pump one, and the effects mentioned above can significantly affect the gain of the device, ultimately leading to compression, i.e. a significant decrease of the signal gain compared to the linear one (obtained at low input signal power).

In order to experimentally study the causes of compression in a J-TWPA, we implemented the experimental setup shown in Fig. 1(b). It consists of a standard setup widely used to characterize the gain of superconducting TWPA [4, 28–30, 39], where the pump and signal microwave tones are combined at room temperature using microwave (MW) splitters. The signal tone is generated using a VNA, so that its frequency and power can be varied while recording its transmission for different pump parameters. The pump tone, usually generated using a MW source, is generated with another VNA in our setup, allowing to also record its complex transmission. The detailed experimental setup is presented in the Appendix A.

The measurement procedure is the following: the frequency of the signal VNA is swept while that of the pump is kept constant. For each signal frequency, pump and signal transmissions are measured. This is repeated for several signal powers.

A typical data set obtained with this setup is shown in Fig. 1(c). The left panel shows the measured normalized transmission (defined below) S_{21} of the signal tone, in

red, and the one of the pump tone, in blue, as a function of the signal power at the input of the TWPA. We will refer to gain when $S_{21} < 0$ dB, and to depletion or attenuation when $S_{21} < 0$ dB. More precisely, we define the signal gain in dB as $G = \bar{S}_{21}^{(s)}(\text{pump ON}) - \bar{S}_{21}^{(s)}(\text{pump OFF})$, where $\bar{S}_{21}^{(s)}$ is the raw measured transmission through the whole setup with the signal VNA. Similarly, the pump transmission in dB is defined as $S_{21} = \bar{S}_{21}^{(p)}(\text{signal ON}) - \bar{S}_{21}^{(p)}(\text{signal OFF})$, $\bar{S}_{21}^{(p)}$ is the raw measured transmission with the pump VNA. The vertical dashed line shows the 1-dB compression point defined as

$$P_{1\text{dB}} = P_{\text{sig}}(G_{\text{lin}}^{\text{dB}} - 1 \text{ dB}) \quad (1)$$

where $G_{\text{lin}} = G(P_{\text{sig}} \rightarrow -\infty)$ is the linear gain of the TWPA at low input signal power P_{sig} . One can clearly see that, as the signal gain drops, so does the pump transmission. We attribute this attenuation to a non-negligible pump depletion. The right panel shows gain profiles of the amplifier as a function of the signal frequency for a low and higher P_{sig} in dark and bright red, respectively. The dark and bright blue curves show the corresponding pump transmission profiles as a function of the signal frequency and same P_{sig} . One clearly sees a significant attenuation of several dB of the pump tone for signal frequencies close to the maxima of the corresponding signal gain.

In order to better understand these results, let us now present the modeling of these data.

III. MODEL OF THE GAIN COMPRESSION

The model we use is based on the coupled-modes equations (CMEs) for the three modes envelopes' propagation. This model has already been widely used to model the gain of different types of TWPA [4, 29–32, 37]. The more detailed derivation of the coupled mode equations for a 4WM SAIL TWPA is recalled in the Appendix C. We will here briefly recall the main steps up to the equations that we solve numerically in this study. We will then give approximate analytical formulae that were already derived in the literature [32, 40].

As usual in this theory, we start from the classical equation of motion for a generalized flux wave $\Phi(x, t)$ traveling in the device:

$$\frac{\partial^2 \Phi}{\partial x^2} + L(\Phi_{\text{ext}})C_J \frac{\partial^4 \Phi}{\partial x^2 \partial t^2} - \frac{L(\Phi_{\text{ext}})C_g}{a^2} \frac{\partial^2 \Phi}{\partial t^2} - \frac{3a^2 \tilde{\gamma}}{I_c^2 L(\Phi_{\text{ext}})^2 \tilde{\alpha}^3} \frac{\partial^2 \Phi}{\partial x^2} \left(\frac{\partial \Phi}{\partial x} \right)^2 = 0. \quad (2)$$

Here, $L(\Phi_{\text{ext}})$ is the flux-dependent inductance of the SAIL loop, C_J is the equivalent Josephson capacitance

of the SAIL loop, C_g is the ground capacitance, I_c the critical current of the large JJ in the SAIL loop, a is

the unit cell length in meters, and $\tilde{\alpha}$, $\tilde{\gamma}$ are flux dependent parameters coming from the Taylor expansion of the SNAIL current-phase relation (see Appendix C for further details). In order to obtain CMEs, we follow the method described in Appendix C. However, unlike it is

usually done to obtain simple analytical expressions for the gain of the signal [31, 32, 37], we do not make any further approximation regarding the relative amplitudes A_j of each wave. We also consider the effect of distributed losses in the model. We finally obtain the following CMEs for the propagation of the three waves envelopes:

$$\begin{cases} \frac{\partial A_s}{\partial x} = -k_s'' A_s + i\alpha_{ss} A_s^2 A_s^* + i\alpha_{si} A_i A_i^* A_s + i\alpha_{sp} A_p A_p^* A_s + i\kappa_{si} A_p^2 A_i^* e^{i\Delta k_l x} \\ \frac{\partial A_i}{\partial x} = -k_i'' A_i + i\alpha_{ii} A_i^2 A_i^* + i\alpha_{is} A_s A_s^* A_i + i\alpha_{ip} A_p A_p^* A_i + i\kappa_{is} A_p^2 A_s^* e^{i\Delta k_l x} \\ \frac{\partial A_p}{\partial x} = -k_p'' A_p + i\alpha_{pp} A_p^2 A_p^* + i\alpha_{pi} A_i A_i^* A_p + i\alpha_{ps} A_s A_s^* A_p + i\kappa_{psi} A_s A_i A_p^* e^{-i\Delta k_l x} \end{cases} . \quad (3)$$

The coefficients α_{jj} are the self-Kerr coefficients, α_{jk} are the cross-Kerr coefficients, and the κ 's are the 4WM coefficients ruling the energy exchange between the different waves. Their expressions are given in Appendix C. The first term accounts for propagative losses via $k_j'' = \tan(\delta)k_j/2$ with $\tan(\delta)$ the loss tangent of TWPA, and $\Delta k_l = 2k_p - k_s - k_i$ is the linear phase mismatch. These equations are formally equivalent to those already derived for optical parametric amplifiers [40–42], or superconducting TWPA [31, 32]. It should be noted that, with further approximations, analytical formulae can be obtained for propagation $A_j(x)$ including pump depletion effects [32, 41]. However, we will not use them in this work as they do not account for losses, and rely on Jacobi elliptic functions, thus not showing explicit dependence with the powers, non-linear coefficients, or phase-mismatch.

We then numerically solve these equations as a function of the position x in the TWPA, and we define the gain of the signal and the transmission of the pump as

$$\begin{aligned} \bar{S}_{21}^{(s)} &= |A_s(x = L)/A_s(0)|^2 \\ \bar{S}_{21}^{(p)} &= |A_p(x = L)/A_p(0)|^2 \end{aligned} \quad (4)$$

respectively. We also compute these transmissions without pump tone ($A_p(0) = 0$), or signal tone ($A_s(0) = 0$), to obtain the reference for normalization of these 'calibrated' transmissions obtained numerically. The difference between the simulations with signal (pump) tone and the ones with $A_p(0) = 0$ ($A_s(0) = 0$) directly correspond to the normalized experimental signal (pump) transmissions defined in section II, and shown in Fig. 1(c).

In Fig. 2, we show the results of these simulations, obtained without any fitting parameters, compared to the experimental data. All input parameters necessary to perform the simulations are the same for 2(a) and (b), obtained from the linear characterization of the device presented in Appendix B and from the calibration of the experimental setup presented in Appendix A. We obtain

a good quantitative agreement between the (smoothed) data and the theory over a wide range of input signal powers, for both the evolution of the gain profile (Fig. 2 (a)) and the pump transmission profile (Fig. 2(b)). We stress here that the color ranges encoding the transmission values in the 2D plots are the same for both data and theory. This agreement is also visible in the linecuts shown in Fig. 2(c).

However, some more detailed features are not perfectly reproduced, such as the exact bandwidth of the gain profile, or the frequencies of the pump transmission minima. We attribute these discrepancies to some simplifications of the model, where perfectly power-independent $50\ \Omega$ matching is assumed, not accounting for the stray geometric inductance of aluminum in the device, higher-order terms in the current-phase relation expansion, or position-dependent loss coefficients for example.

In this figure, we also see two interesting features. First, the pump transmission profile is asymmetric with respect to the pump frequency (7.5 GHz). Second, the pump transmission is not minimum, where the linear gain is maximum. This is observed both experimentally and theoretically.

Regarding asymmetry, it is mostly observed in the simulation results as seen in Figs. 2(a) and (b). Although it is seen in the experimental evolution of the gain in Fig. 2(a) at higher signal powers, the noise and ripples in the pump transmission measurements prevent one from concluding whether this behavior also shows up clearly in the data. It is most likely due to the frequency dependence of the losses, which are lower at smaller frequencies. This already gives simulated asymmetric gain profiles for reversed Kerr TWPA without introducing pump depletion in the model [29]. When energy exchange between the pump and the signal/idler is introduced, the asymmetry in the gain profile is mapped onto the pump transmission profiles.

We will keep the discussion concerning the frequency difference between the minimum of pump S_{21} and the maximum of G_{lin} for the next sections, as it requires further discussion of compression to be understood. We

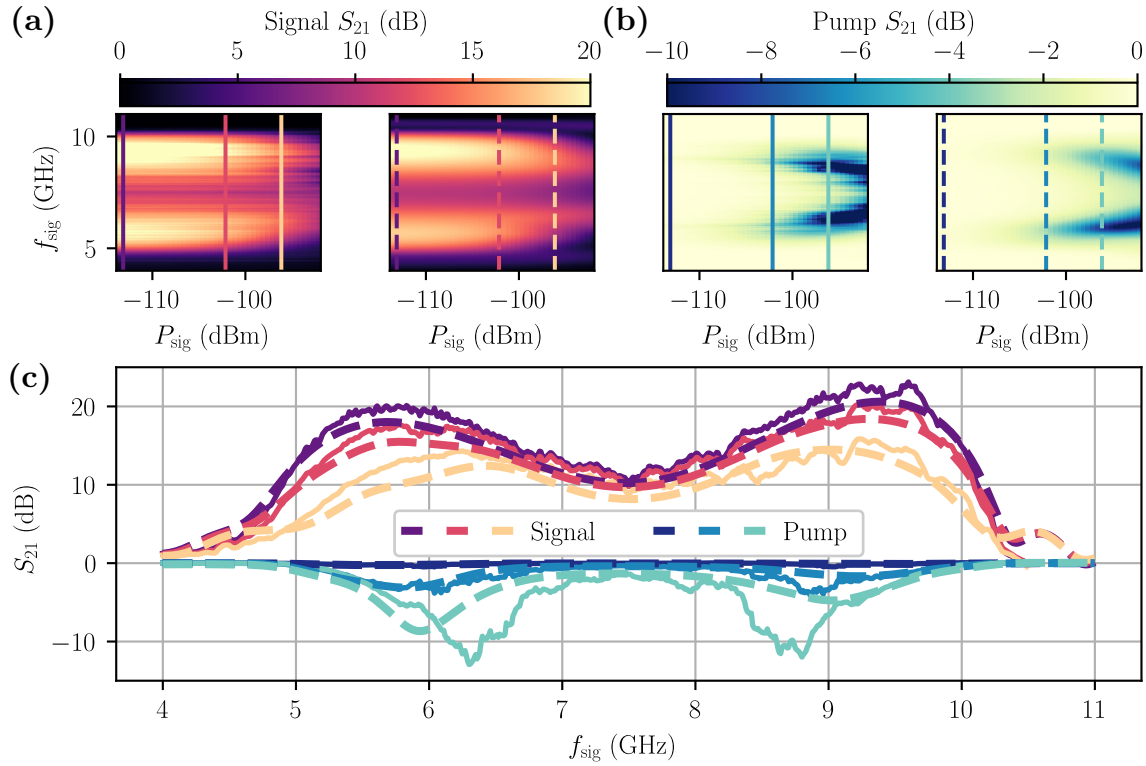


Figure 2. Comparison between experimental data and theory. (a) Measured (left panel) and simulated (right panel) signal gain as a function of the signal frequency and input signal power. (b) Measured (left panel) and simulated (right panel) pump transmission as a function of the signal frequency and input signal power. The vertical lines correspond to the signal powers shown in (c). The simulations contain no fitting parameters and use the same input parameters for both (a) and (b). The axis spans and color ranges are the same for experiment and theory in both (a) and (b). (c) Measured and simulated (plain and dashed lines respectively) signal and pump transmissions (red and blue shades respectively) as a function of the signal frequency for three input signal powers: $P_{\text{sig}} = -113.1$ dBm, -102.1 dBm, and -96.1 dBm (from dark to bright colors respectively). These curves correspond to the vertical linecuts with respective colors in (a) and (b). The experimental data shown in this figure are smoothed as in Fig. 1(c). The pump power is $P_p = -78.4$ dBm.

will now study in more detail the causes of compression in TWPA.

IV. THE 1-DB COMPRESSION POINT

The model we presented earlier was utilized in initial theoretical studies to investigate the causes of compression in a 4WM-based TWPA [31, 32]. In reference [32], the main hypothesis to study signal gain compression is that pump depletion is the only cause. The authors show that, under this hypothesis and the absence of losses, the gain should evolve as

$$G(P_{\text{sig}}) = \frac{G_{\text{lin}}}{1 + 2G_{\text{lin}}P_{\text{sig}}/P_p} \quad (5)$$

where G_{lin} is the linear gain defined in section II, P_p is the input pump power and P_{sig} is the input signal power. This formula should be valid for any kind of 4WM-based TWPA [32, 40, 42].

In Fig. 3(a) we show a comparison between the experimentally obtained $P_{1\text{dB}}$ (red curve), and the ones

obtained from the full simulations using the model of Appendix C, as well as the ones given by Equation (5) in orange and green, respectively. The linear gain G_{lin} used in equation (5) is the one simulated with the full model at the lowest input signal power—hence accounting for losses. The method we used to extract $P_{1\text{dB}}$ from the data is given in Appendix D.

One can see that both theories give an overall good quantitative agreement with the data across the whole bandwidth of the device. However, the two theoretical curves still display quite different features as a function of signal frequency. They both match the data within the central part of the amplification band (between the two vertical dashed lines), and claiming whether one is more accurate than the other is not possible considering the error bars of the measured $P_{1\text{dB}}$ (represented by a light-shaded red curve). They are, however, quite different in the low-frequency part of the amplification band, where the full model matches the data well, while the simplified model does not.

A striking feature in both experiment and full theory is that $P_{1\text{dB}}$ is not the lowest at the frequencies where the

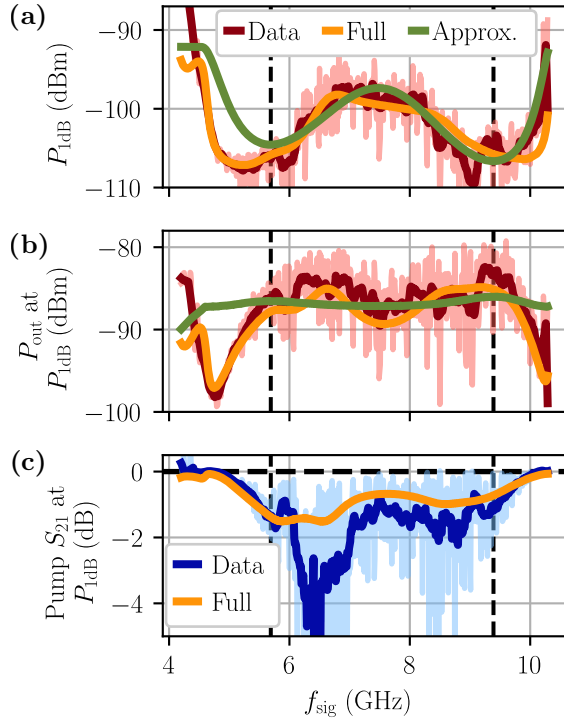


Figure 3. Frequency dependence of the 1-dB compression point and pump transmission at P_{1dB} . (a) P_{1dB} vs signal frequency. The red curve shows the experimentally measured P_{1dB} across the bandwidth of the TWPA. The orange curve shows the theoretical P_{1dB} obtained from simulations with the model presented in Appendix C. The green curve shows P_{1dB} extracted from equation (5) where G_{lin} corresponds to the simulated gain with the full model including losses at the lowest P_{sig} . (b) Output signal power at P_{1dB} as a function of the signal frequency. The colors correspond to the same situations as in (a). (c) The corresponding pump transmission profiles at $P_{sig} = P_{1dB}$ as a function of the signal frequency. The blue curve shows the experimental data and the orange curve shows the simulated pump transmission from the model of Appendix C. In all the figures, the vertical dashed lines highlight the maxima of the signal gain simulated using the full model at the lowest signal power used experimentally. The brighter shaded lines show the raw data while the darker curves correspond to the smoothed data. The pump power is $P_p = -78.4$ dBm.

linear gain is maximum (highlighted by the two vertical dashed lines). However, it is the case for the approximated formula, equation (5), on either side of the pump frequency (7.5 GHz). This can be understood by noticing that the main feature of equation (5) is that P_{1dB} only depends on the linear gain G_{lin} , as already noted in [32]. Therefore, the higher the linear gain, the lower P_{1dB} . This feature is also reproduced in Fig. 3(b), where we show the signal output power P_{out} at the input signal power $P_{sig} = P_{1dB}$ —i.e. $P_{1dB} + G_{lin}^{dB} - 1$ dB. The consequence is an almost flat P_{out} at P_{1dB} as a function of the signal frequency when obtained from equation (5) (green curve), which again matches only the data (red curve)

within the center of the amplification band. Conversely, the output powers at P_{1dB} obtained from the simulations (orange curve) match well the data across the whole band and seem to reproduce slight variations also observed experimentally.

In Fig. 3(c) we show the measured (blue) and simulated (orange) pump transmission at $P_{sig} = P_{1dB}$. The agreement between data and theory is also good (notice the scale difference with respect to Figs. 3(a) and (b)), except for a big dip observed experimentally between $f_{sig} = 6 - 7$ GHz, which is most likely an artifact of the smoothing of the large ripples in the raw transmission profile. However, one clearly observes pump attenuation, *viz.* depletion, of about 1 dB or more, when $P_{sig} = P_{1dB}$. This is observed across the entire bandwidth of the TWPA, except on the edges of the band. This shows that compression is linked to pump depletion in general. However, it cannot explain the detailed behavior of TWPA at the saturation point, as we will discuss hereafter. Still, an interesting conclusion from the analysis of Figs. 3 is that although the expression (5) does not reproduce all the features observed experimentally, it still gives a good quantitative estimate of P_{1dB} for a 4WM TWPA, provided that G_{lin} accounts for losses. However, since Eq. (5) was derived without accounting for them, it could be refined to make losses appear explicitly in gain dependence with signal power.

The main reason why P_{1dB} obtained from Eq. (5) is too approximate, is actually stated in the reference [40] where this expression was originally derived for optical fiber amplifiers. It contains two approximations: (i) low input signal power compared to the total input power, and (ii) valid in the limit of total power conversion between the pump and signal/idler. While the first one is valid even in the regime close to 1-dB compression ($P_{1dB} < -90$ dBm $\ll P_p = -78.4$ dBm), the validity of the second one requires a more detailed analysis of the physics of this non-linear system.

In order to understand with analytical formulae the second approximation, no frequency dependence non-linear coefficients (the equivalent of our α 's and κ 's in Eqs. (3)) has also to be assumed. Following a Lagrangian approach, this allows one to define an optimal, input power-dependent, linear phase mismatch $\Delta k_l^{(opt)}(P_{sig}, P_p)$ at the input of the amplifier that yields total, i.e. asymptotic, power conversion between the pump and signal/idler waves [42]. In the case of our Josephson TWPA, this frequency dependence cannot be neglected. Therefore, the Lagrangian formulation becomes more complex and it is difficult to obtain an equivalent of $\Delta k_l^{(opt)}(P_{sig}, P_p)$ without similar assumptions. However, this explains why Eq. (5) does not reproduce P_{1dB} and P_{out} at P_{1dB} in Figs. 3(a) and (b): it assumes that all frequencies are somehow perfectly phase matched with maximum power conversion efficiency, which is obviously not the case here [29].

Let us now turn to the pump transmission profile at P_{1dB} . Keeping in mind that not all frequencies are

perfectly phase-matched in our device, even at low signal power, and that the total power-dependent phase-mismatch $\Delta\tilde{k}$ is mainly a function of pump power in J-TWPAs [4], an effect of pump depletion is to modify $\Delta\tilde{k}$ during propagation. Thus, on the edges of the band (outside the vertical dashed lines), where no significant pump attenuation is observed, $P_{1\text{dB}}$ in Fig. 3(a) is as low as for the frequencies where G_{lin} is maximum. Since edge frequencies are already initially largely phase mismatched at low P_{sig} by definition, very small variations of the power of any wave during propagation mismatches even more the amplification process, yielding saturation of the gain before the output of the device. The effect of this ‘depletion-induced’ matching modification is illustrated in Fig. 4, where two regions can be identified. In the central part of the bandwidth, there is a stable frequency range where the gain increases monotonically with position inside the device. Conversely, the edges of the band are an instable region where the gain oscillates with position. In other words, for small $\Delta\tilde{k}$ the gain as a function of position is a monotonically increasing function (typically $\propto \cosh(gx)$ where g is some coefficient and x the position [32]), but it becomes a periodic function of position if $|\Delta\tilde{k}|$ is too large yielding an imaginary g [32]. In the specific case of a SNAIL-TWPA operated in the reversed-Kerr regime, depleting the pump tends to lower $\Delta\tilde{k}$, making the central frequencies better phase-matched, but mismatching the frequencies more detuned from the pump. The boundaries between the two regions are difficult to infer but are close to the maxima of the linear gain (vertical dashed lines in Fig. 4), and result from the parameters of the device, pump power and the losses. This yields a complex interplay between lowering the energy available for amplification, and power-induced phase-mismatch with possible coherent, i.e. oscillatory, energy exchange between waves from which results gain compression.

It should be noted that a TWPA with a single Josephson junction as unit cell might display a different behavior for all frequencies as in that case $\Delta\tilde{k}$ is always negative with our conventions, and lowering pump power would shift it towards zero. This also stands for a dispersion engineered TWPA like the one of Ref. [4]. This highlights that the coherent nature of the amplification process inside a TWPA should be considered for accurate modeling of the gain at high input signal power [31].

V. CONCLUSION AND DISCUSSIONS

In this article, we have presented an experimental study of compression in a SNAIL traveling-wave parametric amplifier operated in 4WM. We have implemented a novel experimental setup allowing one to track the pump tone transmission as a function of the signal tone power and frequency.

The study reveals that pump depletion is observed at 1-dB compression and input signal powers beyond.

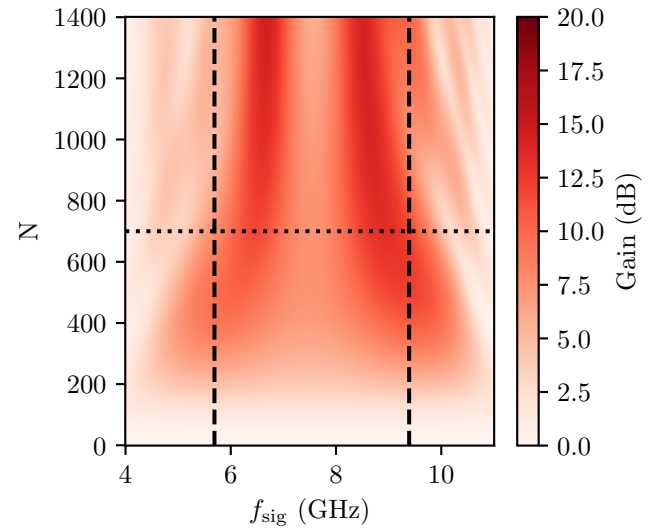


Figure 4. Stability of gain build-up at high signal power. Simulated signal gain as a function of the position inside the TWPA in unit cell number N and signal frequency. The input signal power is $P_{\text{sig}} = -94.6$ dBm. The horizontal dotted line indicates the actual length of the device under study here ($N = 700$). The vertical dashed lines correspond to the two maxima of the simulated linear gain profile.

Using the classical framework of coupled-mode equations, we are able to accurately model the gain and pump transmission profiles for various input signal powers, without any fitting parameters. The comparison between the data and theory shows that a simplified formula (Eq. 5) already obtained previously [32] with the hypothesis that solely pump depletion causes compression—an irreversible energy conversion argument, gives the good order of magnitude to model the 1-dB compression point of such a TWPA. However, one needs to simulate the entire system beyond some of the approximations yielding Eq. (5) to capture more detailed features of the frequency dependence of $P_{1\text{dB}}$ and the corresponding pump transmission profile. This treatment encompasses the effect of losses and power-induced variations of the phase-matching $\Delta\tilde{k}$ during propagation yielding oscillatory behavior of the modes envelopes. When the measured signal gain and pump transmission decrease monotonically as a function of input signal power, compression is mainly due to pump depletion where significant linear gain is observed. Yet, pump-depletion induced $\Delta\tilde{k}$ causes compression for the frequencies being already largely phase-mismatched at low input signal power.

It is straightforward that the main limitation is the amount of pump power that can be fed to the device. Therefore, in order to increase the 1-dB compression point of 4WM-based J-TWPAs, Josephson junctions with larger critical current should be used. Engineering of the TWPA (dispersion relation, optimal length) should obviously be performed to compensate for the resulting

lower non-linearity of each unit cell.

Second, given that the bandwidth of TWPA is large and the gain usually not constant, so is $P_{1\text{dB}}$. Therefore, for applications such as multiplexed qubit readout where the large input power comes from several low-power signals at different frequencies, these tones could be concentrated in frequency bands where $P_{1\text{dB}}$ is higher, such as frequencies closer to the pump in the case of the SNAIL-TWPA studied here. In this way, one stays far from the regime close to compression with significant generation of unwanted intermodulation products and sidebands [15].

We believe that our study confirms existing theoretical predictions and will help designing TWPAAs with larger 1-dB compression points, paving the way towards efficient setups for multiplexed qubit readout, a key requirement for scaling up quantum circuits.

ACKNOWLEDGMENTS

This project has received funding from the European Union's Horizon 2020 research and innovation programme within the project AVaQus (grant agreement number 899561), from European Union's Horizon Europe 2021-2027 project TruePA (grant agreement number 101080152), and from the French ANR-22-PETQ-0003 grant under the 'France 2030' plan. B.F. acknowledges the QMIC project under the program DOS0195438/00. We would like to acknowledge M. Esposito for her significant assistance with the sample fabrication. The sample was fabricated at the clean room facility *Nanofab* of Institut Néel in Grenoble. We thank the clean room staff and L. Cagnon for their assistance with the device fabrication. We express our gratitude to, J. Jarreau, L. Del Rey, D. Dufeu, F. Balestro, and W. Wernsdorfer for their support with the experimental equipment. We are also grateful to the superconducting quantum circuits group members at Institut Néel for helpful discussions. We thank Q. Ficheux and R. Albert for their critical reading and constructive feedback on the manuscript.

G.L.G., G. B., and N.R. conceptualized the experiment. A.R. fabricated the device. G.L.G. and G.B. measured in the cryogenic setup with the help of A.R., B.F. and G.C. L.P., E.B., E.E. and N.R. provided support with the measurement setup. G.L.G. performed data curation with the help of G.B., A.R., B.F., G.C. and N.R. G.L.G. performed the formal analysis. G.L.G., and N.R. drafted the article with contributions from all the authors.

Appendix A: Experimental setup

The device is mounted in a copper box and connected to a $50\ \Omega$ copper coplanar waveguide (CPW) using aluminum wire bonds. The box is anchored along with a coil for DC flux bias to the mixing chamber of a dilution fridge and operated at a temperature close to 20 mK.

It is placed inside a μ -metal magnetic shield. The amplifier is followed by two single-junction isolators, and a High-Electron-Mobility-Transistor (HEMT) low-noise amplifier anchored at the 4K stage of the fridge.

The complete experimental setup used in this study is shown in Fig. 5(a). As compared to usual setups used for characterizing TWPA, we use a second VNA at room temperature for generating the pump tone and measuring its transmission as discussed in the main text (section II). In addition, at the base temperature of the dilution fridge, the sample is 'sandwiched' between two directional couplers at input and output in order to measure the full scattering matrix of the device. Reflection measurements are not used in this study.

In order to perform all the calibration needed for the study, we did several cooldowns with different samples:

1. Thermal noise source at output A and an open cable at output B. This allows calibrating the system gain of output line A and the base reflection of output line B.
2. Open cable at output A and thermal noise source on output B. This is the reciprocal of the first cooldown.
3. Dummy 'PCB' sample in between the two directional couplers. It is an on-chip $50\ \Omega$ matched copper coplanar-waveguide transmission line. The packaging used is the same as for the TWPA (copper box, connectors and wire-bonding). It is used to calibrate the transmission of the lines and provides a reference for the linear characterization of the TWPA as discussed in section B.
4. SNAIL TWPA in between the two directional couplers with its coil to apply DC magnetic flux to the sample.

In between all these cooldowns, nothing else than the different devices facing the two directional couplers was modified.

In order to obtain the input line attenuation of our input line and estimate accurately the powers at the input of the TWPA, we used a thermal noise source to calibrate our output system gain. We then subtract it to the full transmission across the fridge measured on the PCB sample to obtain the input line attenuation including losses of the packaging. The error made on this estimation is thus solely the intrinsic losses of the PCB transmission line and on one side of the packaging.

The thermal noise source is a cryogenic $50\ \Omega$ cap, and is anchored to a copper mount held by a thin copper wire providing a thermal weak link to the mixing chamber plate. The RF output of the cap is connected to the outputs of the fridge using a superconducting micro-wave cable. In this way, it could thermalize down to 200 mK during the cooldown, and when heated up to calibrate the gain, it does not heat up in return the mixing chamber

plate. A thermometer and a heater are also anchored to the copper mount.

To perform the calibration, we measure the noise power emitted by the source at different temperatures. We then fit the data for each frequency using the model for the measured power in watts at room temperature:

$$P(\omega) = (N_{\text{source}} + N_{\text{sys}}) G_{\text{sys}} \Delta f k_B \quad (\text{A1})$$

where Δf is the integration bandwidth, N_{sys} and G_{sys} are respectively the noise temperature (in K) and total gain of the system. The noise temperature in K emitted by the thermal source (N_{source}) is modeled as

$$N_{\text{source}} = \frac{\hbar\omega}{2k_B} \coth\left(\frac{\hbar\omega}{2k_B T_s}\right) \quad (\text{A2})$$

where T_s is the source temperature. The result of the gain calibration along with estimation of the input line attenuation is shown in Fig. 5(b).

We show in Fig. 5(b) some examples of these fits, as well as the resulting system gain calibration and estimated input-line attenuation for both the signal line and the pump line (different because of the extra attenuator used with the signal VNA at room temperature as shown in Fig. 5(a)).

Appendix B: Device fabrication and linear characterization

Fabrication of the device

The device under study here was fabricated in the clean room of the Institut Néel. The fabrication steps are identical to those of the device presented in the reference [29]. We here briefly recall the main steps.

First, the Josephson junctions and Aluminum bridges constituting the SNAIL array are patterned using electron-beam lithography and evaporated using a double-angle shadow evaporation Dolan bridge technique. Then, a thin layer (~ 25 nm) of Aluminum Oxyde is deposited on the whole wafer using atomic-layer deposition. Finally, a thick layer of Copper is deposited on top of the wafer, except for the bounding pads, to form the ground capacitance of the array.

Linear characterization

In order to estimate all the parameters necessary to model the data we measure the linear parameters of the device. To do so, we measure the device's transmission as a function of the flux threading the SNAIL loops. We then subtract the transmission measured on the PCB sample, assumed to be lossless with respect to the device's attenuation. The S_{21} parameter's magnitude and

phase are normalized in order to obtain the losses as a function of frequency and the linear dispersion relation, respectively:

$$|S_{21}(\Phi_{\text{ext}})| = \left|S_{21}^{(\text{DUT})}(\Phi_{\text{ext}})\right| / \left|S_{21}^{(\text{PCB})}\right|, \quad (\text{B1})$$

$$\theta(\Phi_{\text{ext}}) = \theta^{(\text{DUT})}(\Phi_{\text{ext}}) - \theta^{(\text{PCB})}. \quad (\text{B2})$$

We first fit $\theta(\Phi_{\text{ext}})$ with a general function for the dispersion relation:

$$\theta(\Phi_{\text{ext}}) = \theta_0(\Phi_{\text{ext}}) + \frac{N\omega\sqrt{L(\Phi_{\text{ext}})C_g}}{\sqrt{1 - L(\Phi_{\text{ext}})C_J\omega^2}} \quad (\text{B3})$$

where $\theta_0(\Phi_{\text{ext}})$, $L(\Phi_{\text{ext}})$, C_g and C_J are fitting parameters. As an outcome of this fit we only retain the parameter $\theta_0(\Phi_{\text{ext}})$ and use it to rescale the absolute phase of the first measured frequency of the VNA traces. The absolute wave vectors $k(\Phi_{\text{ext}})$ are then defined as

$$k(\Phi_{\text{ext}}) = \frac{\theta(\Phi_{\text{ext}}) + \theta_0(\Phi_{\text{ext}})}{l}, \quad (\text{B4})$$

where $l = Na$ is the length of the device with N the number of SNAIL and a the length of one unit cell. Then, we fit the dispersion relation $k(\omega)$ for each flux value using the standard formula

$$k(\omega) = \frac{\omega\sqrt{L(\Phi_{\text{ext}})C_g}}{a\sqrt{1 - L(\Phi_{\text{ext}})C_J\omega^2}} \quad (\text{B5})$$

with only $L(\Phi_{\text{ext}})$ and C_g as fitting parameters. $C_J = 31$ fF is known from fabrication and corresponds to the equivalent Josephson capacitance of the SNAIL loop. As an outcome of this fit, a flux-dependent C_g is obtained as shown in Fig. 6(b), which is not physical as the dependence with flux of $k(\omega)$ is expected to be only due to the variation of the inductance $L(\Phi_{\text{ext}})$. We therefore fix C_g to the mean value obtained from this fit, and fit again the dispersion relation with equation (B5) and $L(\Phi_{\text{ext}})$ as the only fitting parameter. The result is shown in Fig. 6(a).

In order to estimate the ratio r and the critical current of the large junctions I_c , we then fit the dependence of the inductance with the external flux with the expected variation of the linear inductance of the SNAIL loop from the current-phase relation expansion:

$$L(\Phi_{\text{ext}}) = \frac{\varphi_0}{\tilde{\alpha}(\Phi_{\text{ext}})I_c} \quad (\text{B6})$$

where $\tilde{\alpha}(\Phi_{\text{ext}})$ is defined in equation (C3) and $\varphi_0 = \hbar/(2e)$ the reduced flux quantum. The fit is shown in Fig. 6(c) and we obtain $r = 0.062$ and $I_c = 1.4 \mu\text{A}$.

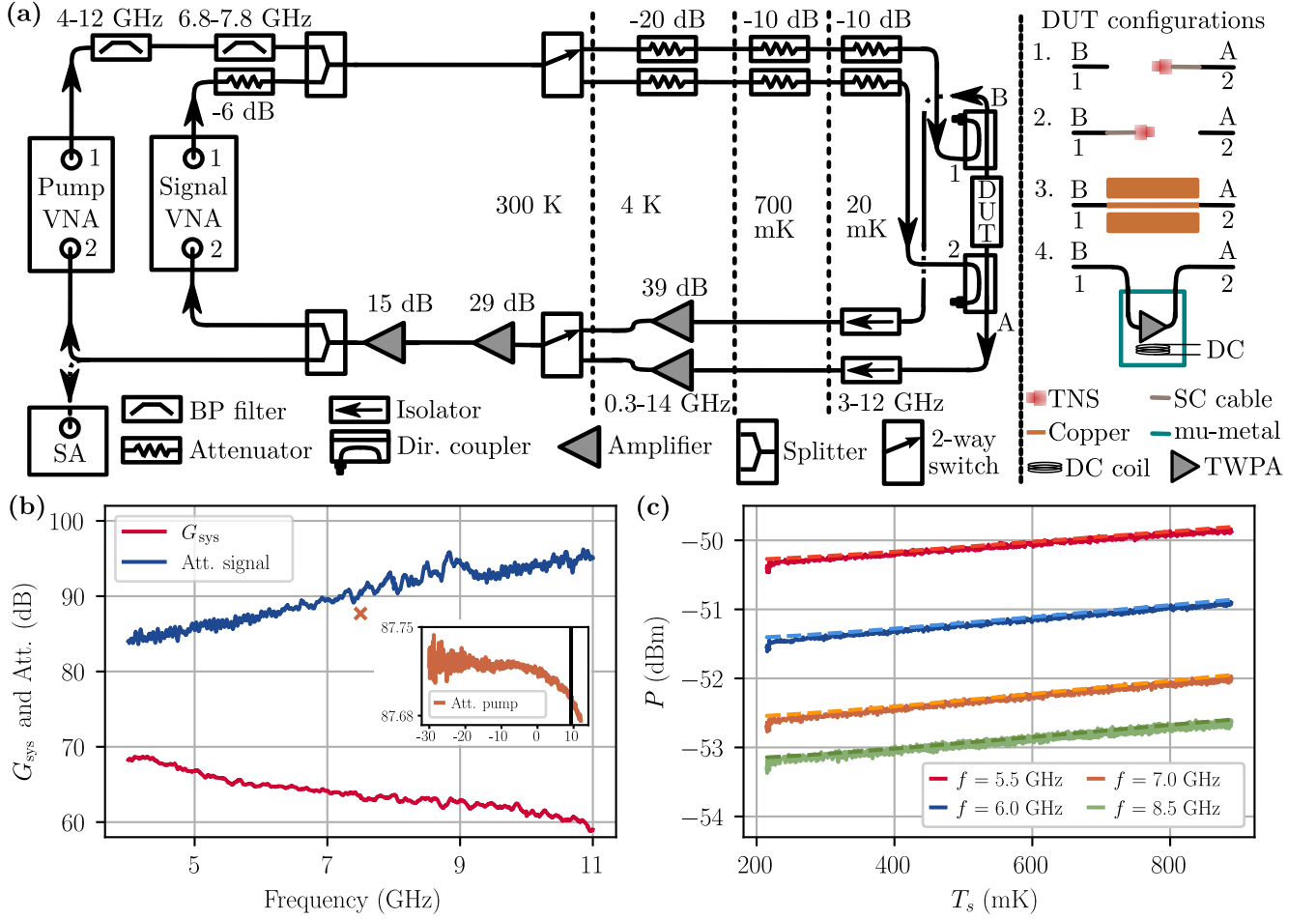


Figure 5. Experimental setup and system calibration. (a) Full experimental setup. ‘DUT’ (device under test) corresponds to the different configurations depicted on the right and explained in the main text. BP: band-pass, SA: spectrum analyzer, SC: superconducting, TNS: thermal noise source (a cryogenic $50\ \Omega$ cap), VNA: vector network analyzer. For simplicity, we represent only one isolator but two are used on each line to provide ~ 40 dB isolation. A & B label the outputs while 1 & 2 label the inputs on the right panel. The directional couplers have 20 dB attenuation on the coupled port. (b) System gain (red) as a function of frequency and the resulting input line attenuation for the signal line (blue) obtained with configuration 3 in (a) minus G_{sys} (both in dB). The orange cross shows the attenuation of the pump line at the pump frequency $f_p = 7.5$ GHz. **Inset:** Input line attenuation in dB for the pump line as a function of the pump VNA power in dBm. The vertical line shows the VNA power used for all the measurements presented in this article. (c) Examples of power emitted by the TNS when varying the temperature of the stage it is anchored to (plain lines), along with the fits (dashed lines) used to obtain G_{sys} in (a) from Eq. (A1).

The last parameter needed for the simulations is the loss tangent $\tan(\delta)$. Before describing the procedure to extract it, let us make a few comments. The main loss process we expect for our device is dielectric losses located in the dielectric forming the top ground (see above for fabrication details and reference [43]). In superconducting circuits operated in the microwave regime, such losses are usually attributed to the excitation of two-level systems (TLS) which brings power-dependent losses [43]. In our device, this power dependence is also observed, and the typical evolution of $|S_{21}|$ versus power at a given frequency is very similar to the one of the internal quality factor of a resonator versus the average number of photons inside. Since we extensively study the properties

of our device over a broad range of powers (more than 20 dBm), we therefore need to account for the power dependence of the loss tangent to accurately model our data. In addition, we need it for the signal and idler, but also for the pump whose power is much larger than the one of the signal. In order to obtain the most accurate estimation for the pump at the right power and for the signal at all the powers presented in this article, we extract $\tan(\delta)$ on two different kinds of data with the same procedure. Let us first present the procedure.

The attenuation in a transmission line is usually modeled as follows in linear units [43, 44]:

$$A(x, \omega) = e^{\alpha_d(\omega)x} \quad (B7)$$

with

$$\alpha_d(\omega) = \frac{k(\omega) \tan(\delta)}{2}. \quad (B8)$$

Therefore, $\tan(\delta)$ can be obtained by fitting the transmission versus $k(\omega)$. This definition of the attenuation coefficient is in Np/m. Thus, from the fit of $|S_{21}(\omega)|$ in dB versus $k(\omega) \times L$ (or equivalently the measured absolute phase) with a linear relation $S_{21}^{\text{dB}} = k(\omega)L\alpha_{\text{fit}}$ we obtain the loss tangent as defined above as:

$$\tan(\delta) = \alpha_{\text{fit}} \times 2 \ln(10)/20 \quad (B9)$$

where α_{fit} is the fitted slope in dB/rad.

The results of these fits for transmission traces as a function of the RT VNA power are shown in Fig. 6(d). To estimate $\tan(\delta)$ at the pump power used, we take the value obtained at the largest RT VNA power used, the closest to the pump power¹.

To estimate the value of $\tan(\delta)$ at the different powers used for the signal, we fit composite $|S_{21}|$ versus phase data, where each $|S_{21}|$ trace is reconstructed so that for each frequency the input power at the device is the same as explained in Appendix D. In both cases however, the phase data used for these fits are the same for all the powers, coming from the dataset used to fit the dispersion relation shown in Fig. 6(a) at $\Phi_{\text{ext}} = \Phi_0/2$. This choice was made to avoid possible (although negligible in our data) phase shift due to self-Kerr effect that could modify $k(\omega)$ and add a correction to $\tan(\delta)$ while we want to obtain the linear loss tangent.

Appendix C: Theoretical modeling based on coupled-mode equations

The model we use to compare to our data is based on the widely used coupled-mode equations (CME) for simulating the gain of the TWPA. The equation of motion (2) is obtained by applying Kirchoff's current law at each node of the lumped-element model of the SAIL chain. We use the following current phase relation for the SAIL:

$$I = rI_c \sin(\Phi/\varphi_0) + I_c \sin\left(\frac{\Phi - \Phi_{\text{ext}}}{3\varphi_0}\right) \quad (C1)$$

¹ We could not measure directly transmission traces with the pump VNA to estimate more precisely $\tan(\delta)$ at the pump power used in the experiments.

where $\Phi = \varphi_0\phi$ is the generalized flux for ϕ the superconducting phase difference across the SAIL. It is further expanded around a flux Φ^* such that $I(\Phi^*) = 0$ as

$$\begin{aligned} I(\Phi^* + \delta\Phi) &\approx \frac{I_c}{\varphi_0} \left[r \cos\left(\frac{\Phi^*}{\varphi_0}\right) + \frac{1}{3} \cos\left(\frac{\Phi^* - \Phi_{\text{ext}}}{3\varphi_0}\right) \right] \delta\Phi \\ &- \frac{I_c}{6\varphi_0^3} \left[r \cos\left(\frac{\Phi^*}{\varphi_0}\right) + \frac{1}{27} \cos\left(\frac{\Phi^* - \Phi_{\text{ext}}}{3\varphi_0}\right) \right] \delta\Phi^3 + O(\delta\Phi^5) \end{aligned} \quad (C2)$$

where we already dropped the terms independent of $\delta\Phi$ and proportional to $\delta\Phi^2$, anticipating that we will work at $\Phi_{\text{ext}} = \Phi_0/2$ where the coefficients are zero [23, 45]. By defining the coefficients $\tilde{\alpha}$ and $\tilde{\gamma}$ as

$$\tilde{\alpha} = r \cos\left(\frac{\Phi^*}{\varphi_0}\right) + \frac{1}{3} \cos\left(\frac{\Phi^* - \Phi_{\text{ext}}}{3\varphi_0}\right) \quad (C3)$$

$$\tilde{\gamma} = \frac{1}{6} \left[r \cos\left(\frac{\Phi^*}{\varphi_0}\right) + \frac{1}{27} \cos\left(\frac{\Phi^* - \Phi_{\text{ext}}}{3\varphi_0}\right) \right] \quad (C4)$$

and $L(\Phi_{\text{ext}}) = L_J/\tilde{\alpha} = \varphi_0/(\tilde{\alpha}I_c)$ this yields the equation of motion (2) in the continuous limit. In practice, $\tilde{\alpha}$ and $\tilde{\gamma}$ are obtained by solving equation (C1) at the Φ_{ext} of interest.

Then, we use the following Ansatz to solve equation (2):

$$\Phi = \frac{1}{2} \sum_{j \in \{p, s, i\}} \left(A_j(x) e^{i(k_j x - \omega_j t)} + A_j^*(x) e^{-i(k_j x - \omega_j t)} \right), \quad (C5)$$

where A_j is the slowly varying amplitude in units of flux (Wb) of the mode j along x ; p , s , i respectively denote the pump, signal and idler modes with k_j and ω_j their associated wave-vectors and angular frequencies. To solve the equation of motion, we perform the following approximations:

- $|\partial^2 A_j / \partial x^2| \ll |k_j \partial A_j / \partial x|$ in the linear terms,
- $|\partial^2 A_j / \partial x^2 / k_j|, |\partial A_j / \partial x| \ll |k_j A_j|$ in the non-linear term,
- rotating-wave approximation by forcing the energy conservation $2\omega_p = \omega_s + \omega_i$ and retaining only the time-independent terms,

to obtain the CME (3) for the spatial variation of the three modes envelopes and their complex conjugates. In these equations, the non-linear coefficients are defined as

$$\alpha_{jm} = \frac{6\tilde{\gamma}}{\tilde{\alpha}^3} \frac{a^4 k_m^2 k_j^3}{8C_g I_c^2 L (\Phi_{\text{ext}})^3 \omega_j^2} \quad j \neq m, \quad (C6)$$

$$\alpha_{jj} = \frac{6\tilde{\gamma}}{\tilde{\alpha}^3} \frac{a^4 k_j^5}{16C_g I_c^2 L (\Phi_{\text{ext}})^3 \omega_j^2}, \quad (C7)$$

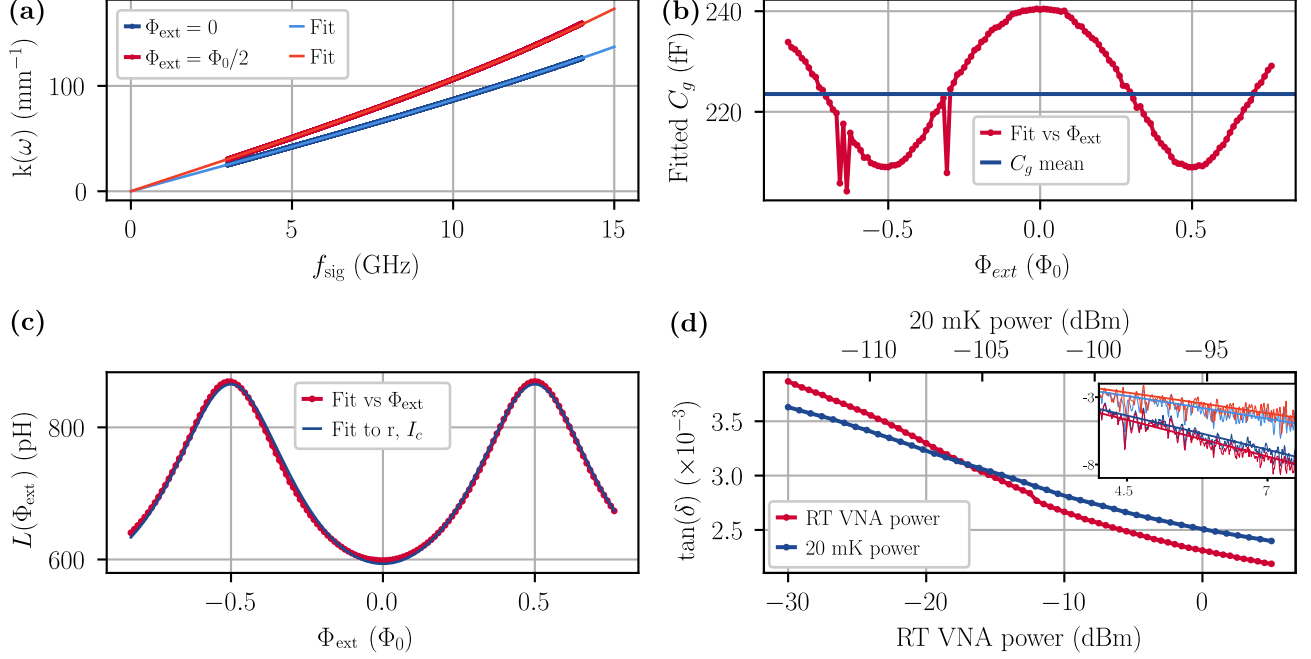


Figure 6. Linear characterization of the device. (a) Dispersion relation of the device extracted from phase measurements at two external magnetic fluxes along with the corresponding fits using Eq. (B5) with only $L(\Phi_{\text{ext}})$ as fitting parameters. (b) Fitted ground capacitance C_g versus Φ_{ext} with 2 fitting parameters in Eq. (B5) and the mean value used as a fixed parameters for the final fit of $L(\Phi_{\text{ext}})$ and the simulations. (c) Fitted values $L(\Phi_{\text{ext}})$ versus Φ_{ext} with only one fitting parameter in Eq. (B5) in red along with the fit to estimate r and I_c in blue from Eq. (B6). (d) Fitted $\tan(\delta)$ from $|S_{21}|$ versus $k(\omega)$ for different input powers. Data in red correspond to fits of raw transmissions for different RT VNA powers (bottom axis), while blue data correspond to fits of reconstructed transmissions for similar input power at each frequency (upper axis) as explained in Appendix D. **Inset:** Raw $|S_{21}|$ data in dB versus frequency in both cases (same color code) for the lowest power (dark colors) and the largest power (brighter colors) of the main figure along with the transmission calculated from the respective fitted $\tan(\delta)$.

$$\kappa_{jm} = \frac{6\tilde{\gamma}}{\tilde{\alpha}^3} \frac{a^4 k_s k_i k_p^2 (2k_p - k_m)}{16 C_g I_c^2 L(\Phi_{\text{ext}})^3 \omega_j^2}, \quad (\text{C8})$$

$$\kappa_{psi} = \frac{6\tilde{\gamma}}{\tilde{\alpha}^3} \frac{a^4 k_s k_i k_p^2 (k_s + k_i - k_p)}{8 C_g I_c^2 L(\Phi_{\text{ext}})^3 \omega_p^2}, \quad (\text{C9})$$

and the linear phase-mismatch $\Delta k_l = 2k_p - k_s - k_i$. One can notice that these coefficients are formally equivalent those derived for a single-JJ chain in reference [32] up to replacing the Josephson inductance L_J by $L(\Phi_{\text{ext}})$, and introducing the flux dependent normalization factor $\xi = 6\tilde{\gamma}/\tilde{\alpha}^3$. We introduce propagation losses for each wave phenomenologically by adding a damping term in the RHS of the CME (3)—which amounts to neglecting the effect of losses on the non-linear coupling of the waves and only consider them for the overall propagation, where the imaginary component of the wave-vectors are defined as

$$k_j''(\omega) = \tan(\delta) k_j(\omega)/2. \quad (\text{C10})$$

We then decompose each equation into differential equations onto their real and imaginary parts and solve them numerically versus position x inside the device, with all the parameters in SI units. When comparing to data, we take the last point of the simulation in $x = L$. The initial flux amplitudes are defined as

$$A_{s,p}(0) = \sqrt{P_{\text{sig,p}} Z_0} / \omega_{s,p}, \quad A_i(0) = 0 \quad (\text{C11})$$

with $Z_0 = \sqrt{L(\Phi_{\text{ext}})/C_g}$ the characteristic impedance of the TWPA.

We finally summarize in Tab. I the linear parameters used for the simulations.

Appendix D: Data analysis methods

In order to obtain the data as presented in Figs. 2 and 3, several processing steps were performed from the raw data measured with both VNA. We here detail the different steps.

Parameter	Value	Unit
Number of SNAIL N	700	—
Unit cell length a	8.7	μm
Critical current ratio r	0.062	—
Large junctions critical current I_c	1.4	μA
SNAIL inductance $L(\Phi_{\text{ext}})$	869.6	pH
SNAIL capacitance C_J	31	fF
Ground capacitance C_g	223.5	fF
Pump power P_p	-78.4	dBm
Pump loss tangent $\tan(\delta)$ at P_p	2.19×10^{-3}	—
Signal loss tangent $\tan(\delta)$	see Fig. 6(d)	—
External magnetic flux Φ_{ext}	$\Phi_0/2$	Wb

Table I. Linear parameters of the TWPA used for the simulations. All the flux-dependent parameters are estimated at $\Phi_{\text{ext}} = \Phi_0/2$.

Single input power gain profiles reconstruction

Because of the frequency dependence of the input line attenuation of the fridge at microwave frequencies, a measured gain or pump transmission VNA trace for a given input signal power at room temperature (RT) actually corresponds to different input signal powers referred at the input of the TWPA. In order to ease the data analysis and compare equivalently all the frequencies in the TWPA bandwidth, we chose to reconstruct the gain and pump transmission profiles for a given input signal power referred at the input of the TWPA.

To do so, we first rescale the VNA output powers at the input of the device thanks to the system gain calibration presented in Appendix A. We therefore obtain for each RT power an array of powers $P_{\text{TWPA}}(\omega)$ at the input of the device containing the frequency dependence—or equivalently a matrix $\mathcal{P}(P_{\text{TWPA}}, \omega)$. Since the attenuation globally increases with frequency (see Fig. 5(b)), we then select the maximum power of the $P_{\text{TWPA}}(\omega)$ array corresponding to the smallest RT power, defining the minimum power at the input of the device $P_{\text{sig}}^{(\min)}$ possibly shared by all the frequencies. In the same fashion, we select the minimum power of the $P_{\text{TWPA}}(\omega)$ array corresponding to the highest RT power. This defines the maximum power $P_{\text{sig}}^{(\max)}$ shared by all frequencies. Then, for each frequency, we truncate the corresponding power array to retain all the powers at the input of the device in the range $(P_{\text{sig}}^{(\min)}, P_{\text{sig}}^{(\max)})$ —i.e. truncating $\mathcal{P}(P_{\text{TWPA}}, \omega)$ along the power direction. Doing so, we basically discard all the powers at the input of the TWPA that are not approximately available at all frequencies

(there is scattering because of the non exactly linear input line attenuation). We then define each single input signal power at the input of the device P_{sig} as the average power along the frequency axis of the truncated matrix $\mathcal{P}(P_{\text{TWPA}}, \omega)$ restricted to the range $(P_{\text{sig}}^{(\min)}, P_{\text{sig}}^{(\max)})$. It results an array of powers P_{sig} where transmission data were measured for each of them, or a power close-by. In Fig. 7(a), we show some iso-power cuts of the truncated matrix $\mathcal{P}(P_{\text{TWPA}}, \omega)$ as a function of frequency before averaging as well as the averaged power (horizontal plain lines). One can see that the power scattering is very small, not exceeding ± 0.5 dBm.

We then reconstruct the complex transmission profiles by taking, for each frequency, the raw VNA data at the power at the input of the device the closest to the averaged one P_{sig} .

Extraction of $P_{1\text{dB}}$

As it can be seen in Fig. 1(c) of the main text, the raw gain data are quite noisy and exhibit ripples. Therefore, the resulting curves of gain as a function of input signal power can be quite noisy, mostly at low powers, hindering a consistent and efficient detection of the 1-dB compression point for all the studied frequencies. In order to extract it with more accuracy and automatically for each frequency, we apply a moving average filter on the G vs P_{sig} curves. This smooths the low-power noise. Then, the 1-dB compression is defined by equation (1). Fig. 7(b) shows a comparison between some typical raw G vs P_{sig} curves (plain lines) and the smoothed result (dashed lines). We also apply the same treatment to the quantities studied at $P_{1\text{dB}}$ (pump S_{21} at $P_{1\text{dB}}$ shown in Fig. 3(c) for instance).

Averaged profiles versus signal frequency

In order to compare more consistently the data to the theory and smooth the scattering due to the ripples of the device, we also average the different quantities studied as a function of signal frequency. To this end, the measured transmissions when $f_{\text{sig}} = f_{\text{pump}}$ are removed—this avoids a staircase-like step around f_{pump} because of the high transmission measured at this frequency, and an 11-points moving-average filter is applied on the data. The result on the various quantities studied can be seen in Figs. 1(c) and 3 by comparing the shaded curves and the plain lines.

[1] B. Ho Eom, P. K. Day, H. G. LeDuc, and J. Zmuidzinas, *Nature Physics* **8**, 623 (2012), number: 8.

[2] M. Esposito, A. Ranadive, L. Planat, and N. Roch, *Applied Physics Letters* **119**, 120501 (2021), number: 12.

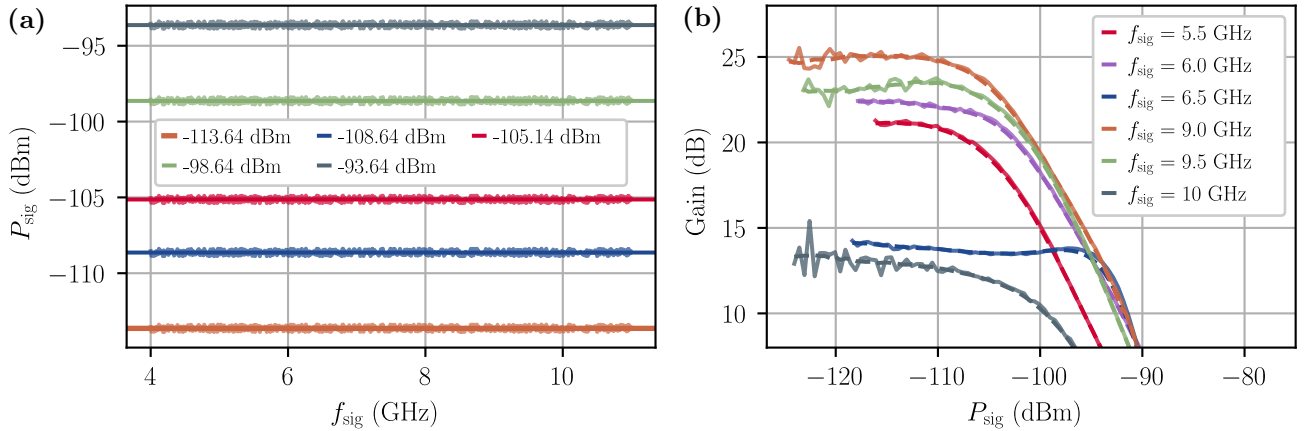


Figure 7. Data processing scattering. (a) Examples of input signal powers across the whole measurement bandwidth and their averages (horizontal plain lines) used to define the input signal powers in this work. (b) Examples of raw (plain lines) and smoothed (dashed lines) signal gain G as a function of the input signal power P_{sig} for different frequencies.

- [3] A. A. Clerk, M. H. Devoret, S. M. Girvin, F. Marquardt, and R. J. Schoelkopf, *Reviews of Modern Physics* **82**, 1155 (2010), number: 2.
- [4] C. Macklin, K. O'Brien, D. Hover, M. E. Schwartz, V. Bolkhovsky, X. Zhang, W. D. Oliver, and I. Siddiqi, *Science* **350**, 307 (2015), number: 6258.
- [5] S. Krinner, N. Lacroix, A. Remm, A. Di Paolo, E. Genois, C. Leroux, C. Hellings, S. Lazar, F. Swiadek, J. Herrmann, G. J. Norris, C. K. Andersen, M. Müller, A. Blais, C. Eichler, and A. Wallraff, *Nature* **605**, 669 (2022).
- [6] W. Ardati, S. Léger, S. Kumar, V. N. Suresh, D. Nicolas, C. Mori, F. D'Esposito, T. Vakhtel, O. Buisson, Q. Ficheux, and N. Roch, *Physical Review X* **14**, 041014 (2024).
- [7] J. Heinsoo, C. K. Andersen, A. Remm, S. Krinner, T. Walter, Y. Salathé, S. Gasparinetti, J.-C. Besse, A. Potočnik, A. Wallraff, and C. Eichler, *Physical Review Applied* **10**, 034040 (2018).
- [8] S. Krinner, S. Storz, P. Kurpiers, P. Magnard, J. Heinsoo, R. Keller, J. Lütolf, C. Eichler, and A. Wallraff, *EPJ Quantum Technology* **6**, 2 (2019).
- [9] L. Ranzani, M. Bal, K. C. Fong, G. Ribeill, X. Wu, J. Long, H.-S. Ku, R. P. Erickson, D. Pappas, and T. A. Ohki, *Applied Physics Letters* **113**, 242602 (2018).
- [10] C. Gaikwad, D. Kowsari, C. Brame, X. Song, H. Zhang, M. Esposito, A. Ranadive, G. Cappelli, N. Roch, E. M. Levenson-Falk, and K. W. Murch, *Physical Review Letters* **132**, 200401 (2024).
- [11] D. De Jong, C. G. Prosko, D. M. A. Waardenburg, L. Han, F. K. Malinowski, P. Krogstrup, L. P. Kouwenhoven, J. V. Koski, and W. Pfaff, *Physical Review Applied* **16**, 014007 (2021).
- [12] V. Elhomsy, L. Planat, D. J. Niegemann, B. Cardoso-Paz, A. Badreldin, B. Klemt, V. Thiney, R. Lethiecq, E. Eyraud, M. C. Dartiallh, B. Bertrand, H. Niebojewski, C. Bäuerle, M. Vinet, T. Meunier, N. Roch, and M. Urdampilleta, *Broadband parametric amplification for multiplexed SiMOS quantum dot signals* (2023), arXiv:2307.14717 [cond-mat].
- [13] D. Fraudet, I. Snyman, D. M. Basko, S. Leger, T. Sepulcre, A. Ranadive, G. Le Gal, A. Torras-Coloma, W. Guichard, S. Florens, and N. Roch, *Physical Review Letters* **134**, 013804 (2025).
- [14] J. O'Sullivan, K. Reuer, A. Grigorev, X. Dai, A. Hernandez-Anton, M. H. Munoz-Arias, C. Hellings, A. Flasby, D. C. Zanuz, J.-C. Besse, A. Blais, D. Malz, C. Eichler, and A. Wallraff, *Deterministic generation of a 20-qubit two-dimensional photonic cluster state* (2024), arXiv:2409.06623 [quant-ph].
- [15] A. Remm, S. Krinner, N. Lacroix, C. Hellings, F. Swiadek, G. J. Norris, C. Eichler, and A. Wallraff, *Physical Review Applied* **20**, 034027 (2023).
- [16] J. Aumentado, *IEEE Microwave Magazine* **21**, 45 (2020), number: 8.
- [17] G. Liu, T.-C. Chien, X. Cao, O. Lanes, E. Alpern, D. Pekker, and M. Hatridge, *Applied Physics Letters* **111**, 202603 (2017).
- [18] L. Planat, R. Dassonneville, J. Puertas Martínez, F. Foroughi, O. Buisson, W. Hasch-Guichard, C. Naud, R. Vijay, K. Murch, and N. Roch, *Physical Review Applied* **11**, 034014 (2019), number: 3.
- [19] O. Naaman, D. G. Ferguson, and R. J. Epstein, *High Saturation Power Josephson Parametric Amplifier with GHz Bandwidth* (2017), arXiv:1711.07549 [physics].
- [20] T. White, A. Opremcak, G. Sterling, A. Korotkov, D. Sank, R. Acharya, M. Ansmann, F. Arute, K. Arya, J. C. Bardin, A. Bengtsson, A. Bourassa, J. Boavard, L. Brill, B. B. Buckley, D. A. Buell, T. Burger, B. Burkett, N. Bushnell, Z. Chen, B. Chiaro, J. Cogan, R. Collins, A. L. Crook, B. Curtin, S. Demura, A. Dunsworth, C. Erickson, R. Fatemi, L. F. Burgos, E. Forati, B. Foxen, W. Giang, M. Giustina, A. Grajales Dau, M. C. Hamilton, S. D. Harrington, J. Hilton, M. Hoffmann, S. Hong, T. Huang, A. Huff, J. Iveland, E. Jeffrey, M. Kieferová, S. Kim, P. V. Klimov, F. Kostritsa, J. M. Kreikebaum, D. Landhuis, P. Laptev, L. Laws, K. Lee, B. J. Lester, A. Lill, W. Liu, A. Locharla, E. Lucero, T. McCourt, M. McEwen, X. Mi, K. C. Miao, S. Montazeri, A. Morvan, M. Neeley,

C. Neill, A. Nersisyan, J. H. Ng, A. Nguyen, M. Nguyen, R. Potter, C. Quintana, P. Roushan, K. Sankaragomathi, K. J. Satzinger, C. Schuster, M. J. Shearn, A. Shorter, V. Shvarts, J. Skruzny, W. C. Smith, M. Szalay, A. Torres, B. W. K. Woo, Z. J. Yao, P. Yeh, J. Yoo, G. Young, N. Zhu, N. Zobrist, Y. Chen, A. Megrant, J. Kelly, and O. Naaman, *Applied Physics Letters* **122**, 014001 (2023).

[21] R. Kaufman, C. Liu, K. Cicak, B. Mesits, M. Xia, C. Zhou, M. Nowicki, J. Aumentado, D. Pekker, and M. Hatridge, *Simple, High Saturation Power, Quantum-limited, RF SQUID Array-based Josephson Parametric Amplifiers* (2024), arXiv:2402.19435 [quant-ph].

[22] C. Eichler and A. Wallraff, *EPJ Quantum Technology* **1**, 2 (2014), number: 1.

[23] N. E. Frattini, V. V. Sivak, A. Lingenfelter, S. Shankar, and M. H. Devoret, *Physical Review Applied* **10**, 054020 (2018), number: 5.

[24] V. V. Sivak, S. Shankar, G. Liu, J. Aumentado, and M. H. Devoret, *Physical Review Applied* **13**, 024014 (2020), number: 2.

[25] B. A. Kochetov and A. Fedorov, *Physical Review B* **92**, 224304 (2015).

[26] S. Boutin, D. M. Toyli, A. V. Venkatramani, A. W. Edidins, I. Siddiqi, and A. Blais, *Physical Review Applied* **8**, 054030 (2017).

[27] C. Liu, T.-C. Chien, M. Hatridge, and D. Pekker, *Physical Review A* **101**, 042323 (2020).

[28] L. Planat, A. Ranadive, R. Dassonneville, J. Puerto Martínez, S. Léger, C. Naud, O. Buisson, W. Hasch-Guichard, D. M. Basko, and N. Roch, *Physical Review X* **10**, 021021 (2020), number: 2.

[29] A. Ranadive, M. Esposito, L. Planat, E. Bonet, C. Naud, O. Buisson, W. Guichard, and N. Roch, *Nature Communications* **13**, 1737 (2022).

[30] M. Malnou, M. Vissers, J. Wheeler, J. Aumentado, J. Hubmayr, J. Ullom, and J. Gao, *PRX Quantum* **2**, 010302 (2021).

[31] O. Yaakobi, L. Friedland, C. Macklin, and I. Siddiqi, *Physical Review B* **87**, 144301 (2013), number: 14.

[32] K. O'Brien, C. Macklin, I. Siddiqi, and X. Zhang, *Physical Review Letters* **113**, 157001 (2014).

[33] C. Kow, V. Podolskiy, and A. Kamal, *Self phase-matched broadband amplification with a left-handed Josephson transmission line* (2022), arXiv:2201.04660 [cond-mat, physics:quant-ph].

[34] A. Y. Levochkina, H. G. Ahmad, P. Mastrovito, I. Chatterjee, G. Serpico, L. Di Palma, R. Ferroiuolo, R. Satariano, P. Darvehi, A. Ranadive, G. Cappelli, G. Le Gal, L. Planat, D. Montemurro, D. Massarotti, F. Tafuri, N. Roch, G. P. Pepe, and M. Esposito, *Superconductor Science and Technology* **37**, 115021 (2024).

[35] J. L. B. Walker, ed., *Handbook of RF and microwave power amplifiers*, The Cambridge RF and microwave engineering series (Cambridge University Press, Cambridge ; New York, 2012).

[36] H. R. Nilsson, D. Shiri, R. Rehammar, A. F. Roudsari, and P. Delsing, *Peripheral circuits for ideal performance of a travelling-wave parametric amplifier* (2024), arXiv:2310.11909 [quant-ph].

[37] L. Planat, *Resonant and traveling-wave parametric amplification near the quantum limit*, Ph.D. thesis, Université Grenoble Alpes, Grenoble (2020).

[38] N. E. Frattini, U. Vool, S. Shankar, A. Narla, K. M. Sliwa, and M. H. Devoret, *Applied Physics Letters* **110**, 222603 (2017), number: 22.

[39] A. Fadavi Roudsari, D. Shiri, H. Renberg Nilsson, G. Tancredi, A. Osman, I.-M. Svensson, M. Kudra, M. Rommel, J. Bylander, V. Shumeiko, and P. Delsing, *Applied Physics Letters* **122**, 052601 (2023).

[40] P. Kylemark, H. Sunnerud, M. Karlsson, and P. A. Andrekson, *Journal of Lightwave Technology* **24**, 3471 (2006).

[41] Y. Chen, *Journal of the Optical Society of America B* **6**, 1986 (1989).

[42] G. Cappellini and S. Trillo, *Journal of the Optical Society of America B* **8**, 824 (1991).

[43] L. Planat, E. Al-Tavil, J. P. Martínez, R. Dassonneville, F. Foroughi, S. Léger, K. Bharadwaj, J. Delaforce, V. Milchakov, C. Naud, O. Buisson, W. Hasch-Guichard, and N. Roch, *Physical Review Applied* **12**, 064017 (2019), number: 6.

[44] D. M. Pozar, *Microwave Engineering*, fourth edition ed. (John Wiley & Sons, Inc, Hoboken, NJ, 2012).

[45] A. Ranadive, *Nonlinear quantum optics with Josephson meta-materials*, Ph.D. thesis, Université Grenoble Alpes (2023).